Chapter II

Single-Ion Magnetic Behavior in Co^{II}–Co^{III} Mixed-Valence Dinuclear and Pseudodinuclear Complexes

---

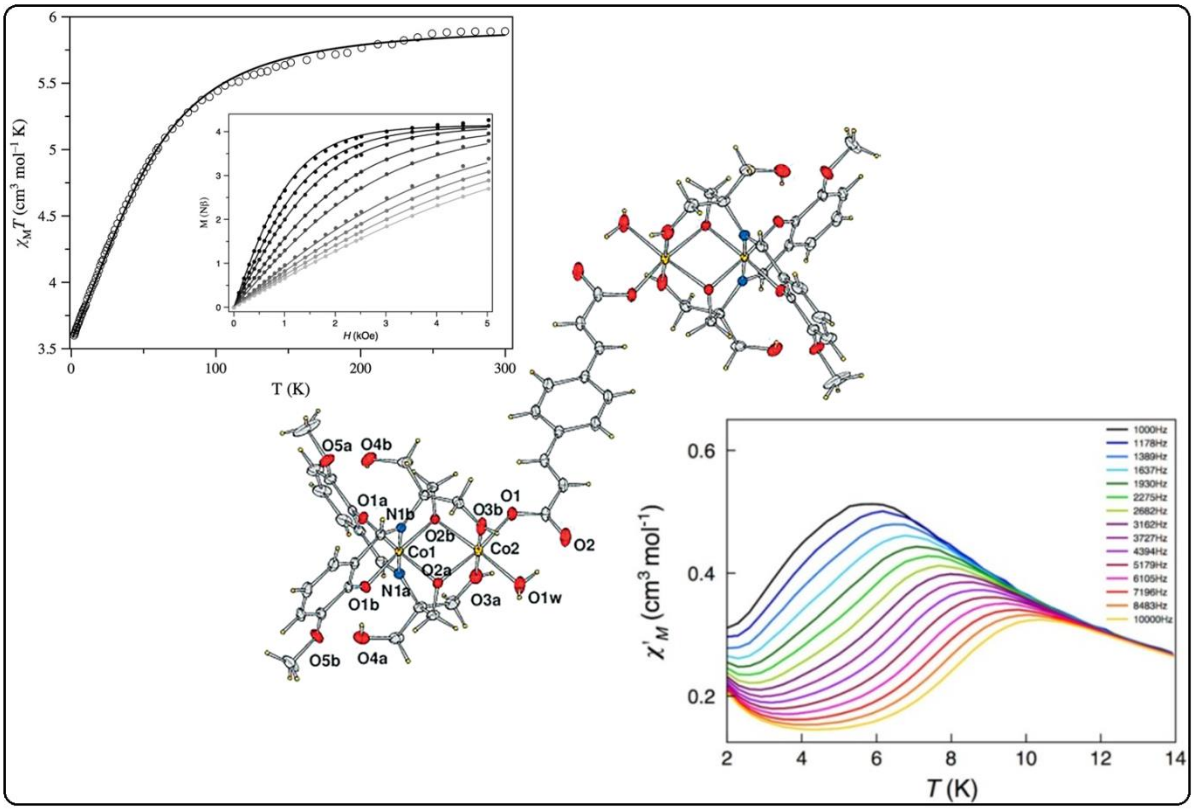

2.1. Introduction

Paramagnetic compounds in which the individual molecules exhibit slow magnetic relaxation and magnetic hysteresis are known as single-molecule magnets (SMMs).[2.1] Since the discovery of the first SMM ($Mn_{12}OAc$) in 1990, much significant work has been done on these magnetic materials due to their potential applications in information storage,[2.2] quantum computing,[2.3] spintronics,[2.4] and magnetic refrigeration.[2.5] The essential requirement for a compound to be a SMM is the presence of a spin-reversal energy barrier between the states with the spin magnetic moments of opposite directions.[2.1a] The spin-reversal barrier is defined as $U=|D|S^2$ and $U = |D|\ (S^2–1/4)$ for integer and half-integer spin moments (S) of the ground states, respectively; D is the axial magnetic anisotropy, which splits the M_S levels of the spin ground state (GS) under zero magnetic field.[2.1a,2.6] Transition-metal-based mononuclear and polynuclear complexes that show SMM behavior have been reported widely in the last two decades.[2.1b,2.7-2.9] The mononuclear compounds with one spin carrier on a molecule, large Ising-type magnetic anisotropy, and magnetic properties similar to those of polynuclear SMMs are usually known as single-ion magnets (SIMs). A literature survey reveals that the major reported SIMs contain late lanthanide ions[2.10] ($4f^n$, n>7), and only a few examples featuring Co^{II},[2.11] Mn^{III},[2.12] Ni^{I},[2.13] Fe^{II},[2.7,2.14] and Fe^{III},[2.15] centers have been reported.[2.16]

Thermally activated slow magnetic relaxation is one of the essential requirements for SMM or SIM behavior. However, from a mixing of the M_s levels promoted by the transverse zero-field splitting (*E,* zfs) and hyperfine or dipolar interactions, this process may be disrupted owing to quantum tunneling of the magnetization (QTM). The mixing of ground degenerate M_s levels through transverse *zfs* is restricted, at least when it comes from a second-order spin-orbit coupling (SOC), for a system with noninteger spin system and negative D value. In this regard, mononuclear cobalt(II) complexes with non-integer spin state (S = 3/2), D< 0, and a forbidden mixing of the ground degenerate M_s levels through transverse *zfs* (*E*) are suitable for a magnet like behaviour.[2.17] However, these rules are not so clear if the *zfs* is derived from a first-order SOC, which is the case for octahedral cobalt(II) complexes; consequently, the existence of cobalt(II) SIMs with positive D values seems to be the norm. Furthermore, mononuclear Co^{II} species can show substantial axial *zfs* (*D*) that can vanish in polynuclear complexes in which the *zfs* tensors of each metal ion are not collinear, as is usually the case. This inconvenience is the main reason why the search for molecules that behave as magnets is focused on mononuclear Co^{II} complexes. However, to date, only a few examples of mononuclear Co^{II} compounds with pseudo-tetrahedral,[2.11b,2.18] octahedral,[2.11c] and square-pyramidal geometries,[2.11a] that show SIM behavior have been reported.

In the present contribution, we report two new Co^{II}-Co^{III} mixed-valence complexes $\{[Co_2(H_2L)_2(H_2O)_2][Co_2(H_2L)_2(H_2O)(m\text{-phth})]\cdot 8(H_2O)\}$ (**1**) and $\{[Co_4(H_2L)_4(H_2O)_2(ppda)]\cdot 2(dmf)\cdot 3.2(H_2O)\}$ (**2**) [where H_2L^{2-} = 2-((2-hydroxy-3-methoxybenzylidene)amino)-2-(hydroxymethyl)propane-1,3-diolato, *m*-phth = 1,3-benzenedicarboxylate; ppda = 1,4-phenylenediacrylate; dmf = N,N-dimethylformamide]. A detailed magnetic study reveals SIM behavior for both compounds.

2.2. Experimental

2.2.1. Materials and Physical Measurements

High-purity 1,4-phenylenediacrylic acid (H_2ppda) (97%) and cobalt(II) acetate tetrahydrate (98%) were purchased from the Aldrich Chemical Co., Inc. and used as received. All other chemicals were of AR grade, and the reactions were performed under aerobic conditions. The solvents used for spectroscopic studies were purified and dried by standard procedures before use.[2.19]

Elemental analyses (carbon, hydrogen and nitrogen) were performed with a Perkin–Elmer 240C elemental analyzer. The IR spectra were recorded with samples as KBr pellets on a

Bruker Vector 22 FTIR spectrophotometer operating from $\tilde{\nu}$ = 400 to 4000 cm^{-1}. The electronic absorption spectra were obtained with a Shimadzu UV-1601 UV/Vis spectrophotometer at room temperature. Quartz cuvettes of 1 cm path length and 3 cm^3 volume were used for all measurements. The ESI-MS spectra of the compounds were recorded in methanol with an Agilent Q-TOF 6500 mass spectrometer, and the Mass Hunter software was used for their analysis. The ^1H and ^{13}C NMR spectra were recorded with a Varian 400 MHz instrument. The X-ray powder diffraction (PXRD) data were collected from Bruker D2 phaser X-ray diffractometer (30 kV, 10 mA), employing Mo-Kα (λ=0.71073Å) radiation at room temperature.

2.2.2. Synthesis

Synthesis of 1 and 2. The complexes **1** and **2** are schematically displayed in Scheme 2.1 with indication of the procedures adopted for their synthesis.

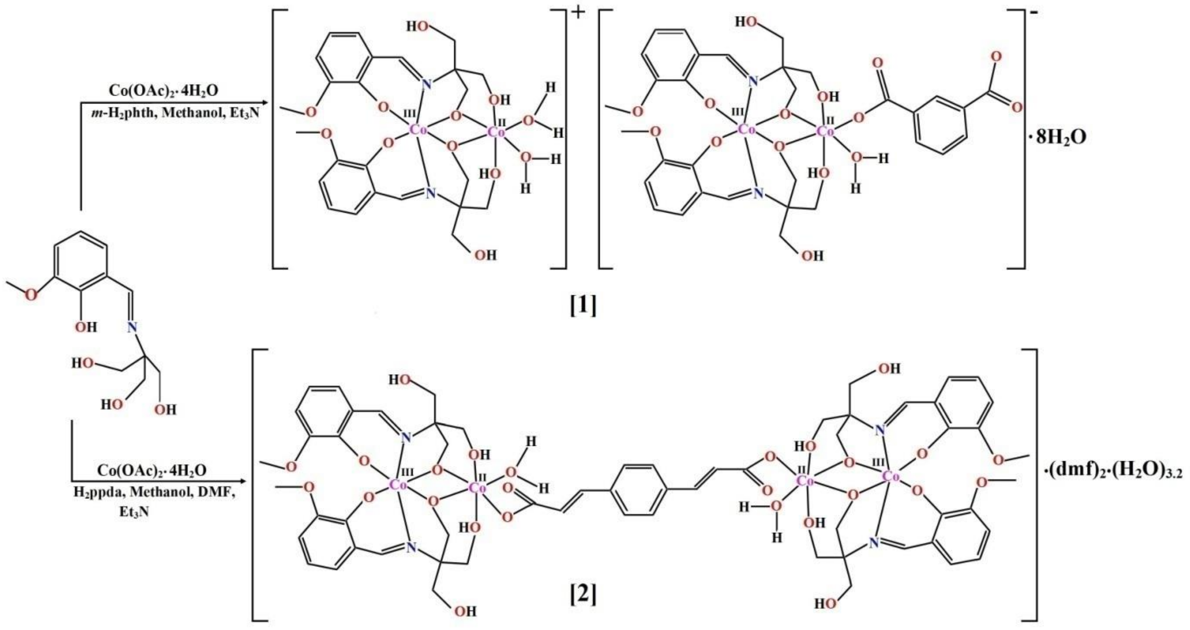

Scheme 2.1. Syntheses of 1-2.

2.2.2.1. Synthesis of 2-[(2-Hydroxy-3-methoxybenzylidene)amino]-2-(hydroxymethyl)propane-1,3-diol (H_4L)

To a stirred methanolic solution (50 mL) of 2-hydroxy-3-methoxybenzaldehyde (0.608 g, 4 mmol), a methanolic solution (50 mL) of tris(hydroxymethyl)amino methane (0.484 g, 4 mmol) was added at room temperature (27°C). The stirring was continued for 2 h. The filtered solution was left for evaporation at room temperature, and a solid yellow compound was obtained after a few days. Yellow crystals of H_4L were collected after recrystallization of the compound in methanol. Yield: 0.714 g (70 %). ESI-MS: *m*/*z* (%) = 256.118 (100) [M + H]$^+$. $C_{12}H_{17}NO_5$ (255.27): calcd. C 56.46, H 6.71, N 5.48; found C 56.44, H 6.70, N 5.51. ^{1}H NMR ([D$_6$]DMSO, 400 MHz): δ = 8.456 (s, 1 H, imine), 6.944, 6.924, 6.890, 6.871 (dd, J = 21.6, 8 Hz, 1 H, Ar), 6.581, 6.563, 6.542 (t, J = 7.6 Hz, 1 H, Ar), 4.907 (s, phenolic OH), 3.611 (s, 6 H, CH_2), 3.718 (s, 3 H, OMe) ppm. ^{13}C NMR ([D$_6$]DMSO, 400 MHz): δ = 164.266 (–CH=N–), 159 (Ar-COMe), 149.754 (Ar-C-OH), 124.343 (Ar-C-imine), 114.551–117.174 (Ar-C), 66.520 (CH_2OH), 61.311 (tertiary carbon), 55.881 (OCH_3) ppm.

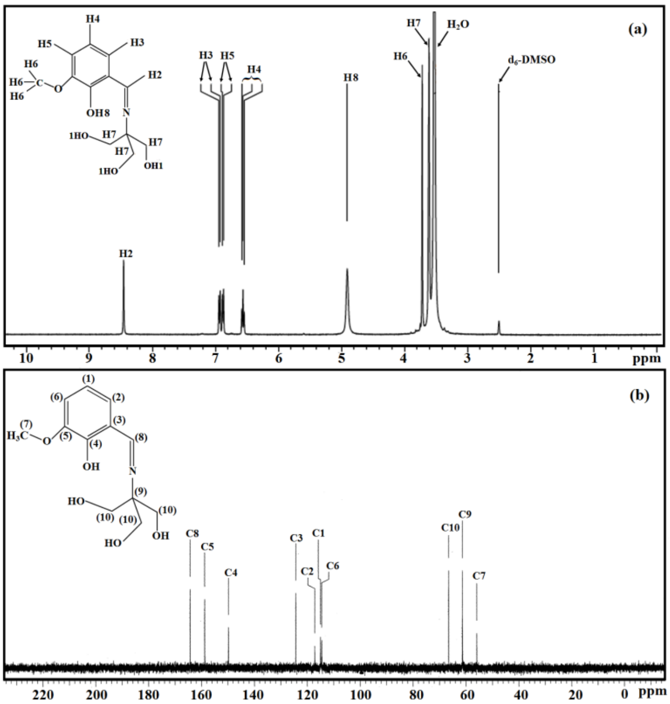

Figure 2.1. ^{1}H NMR (a) and ^{13}C NMR (b) spectra of H_4L.

2.2.2.2. Synthesis of $[Co_2(H_2L)_2(H_2O)_2][Co_2(H_2L)_2(H_2O)(m\text{-phth})]\cdot 8(H_2O)$ (1)

A methanolic solution (20 mL) containing H_4L (0.5 mmol, 0.128 g) and triethylamine (Et_3N) (1 mmol, 0.101 g) was added to a methanolic solution (20 mL) of $Co(CH_3COO)_2 \cdot 4H_2O$ (0.5 mmol, 0.124 g), and the mixture was stirred for 1 h. To the resulting deep brown solution, a mixture of *m*-phthalic acid (0.5 mmol, 0.083 g) and Et_3N (1 mmol, 0.101 g) in methanolic solution (20 mL) was added dropwise, and the stirring was continued for an additional 2 h. Then, the deep brown solution was filtered, and the filtrate was evaporated at room temperature. After 2 d, a brown crystalline compound was collected by filtration. Yield: 0.523 g, 65 %. $C_{56}H_{86}Co_4N_4O_{35}$ (1611.00): calcd. C 41.75, H 5.38, N 3.47; found C 41.72, H 5.41, N 3.49.

2.2.2.3. $[Co_4(H_2L)_4(H_2O)_2(ppda)] \cdot 2(dmf) \cdot 3.2(H_2O)$ (2)

Complex **2** was synthesized by following the same procedure as that adopted for **1** with 1,4-benzenediacrylic acid (0.5 mmol, 0.109 g) instead of *m*-phthalic acid. The filtrate was left at room temperature for slow evaporation. After a few days, a brown compound was collected and dissolved in DMF, and the solution was filtered. Brown crystals suitable for X-ray analysis were obtained after four weeks. Yield: 0.511 g, 60%. $C_{66}H_{92.40}Co_4N_6O_{31.20}$ (1704.77): calcd. C 46.49, H 5.46, N 4.92; found C 46.51, H 5.44, N 4.95.

2.2.3. Crystallographic Data Collection and Refinement

The data collections for **1** and **2** were performed at 120(2) K with Mo-K_α radiation (λ = 0.71073 Å) with an Xcalibur Sapphire3 diffractometer equipped with a CCD detector. The cell refinement, indexing, and scaling of the data sets were performed with the CrysAlisPro package.[2.20] The structures were solved by direct methods with the Olex2 1.2[2.21] software and subsequent Fourier analyses[2.22] and refined by the full-matrix least-squares method on F^2 with all of the observed reflections.[2.22] The hydrogen atoms were placed at calculated positions, except for those of some water molecules, which were detected in the difference Fourier map; however, a suitable H-bonding scheme was difficult to prepare owing to the disordered situation detected in the crystal packing. In **1**, most of the lattice water molecules and the 1,3-benzenedicarboxylate anion share the same site at half occupancy. The crystal data and details of the refinements are given in Table 2.1.

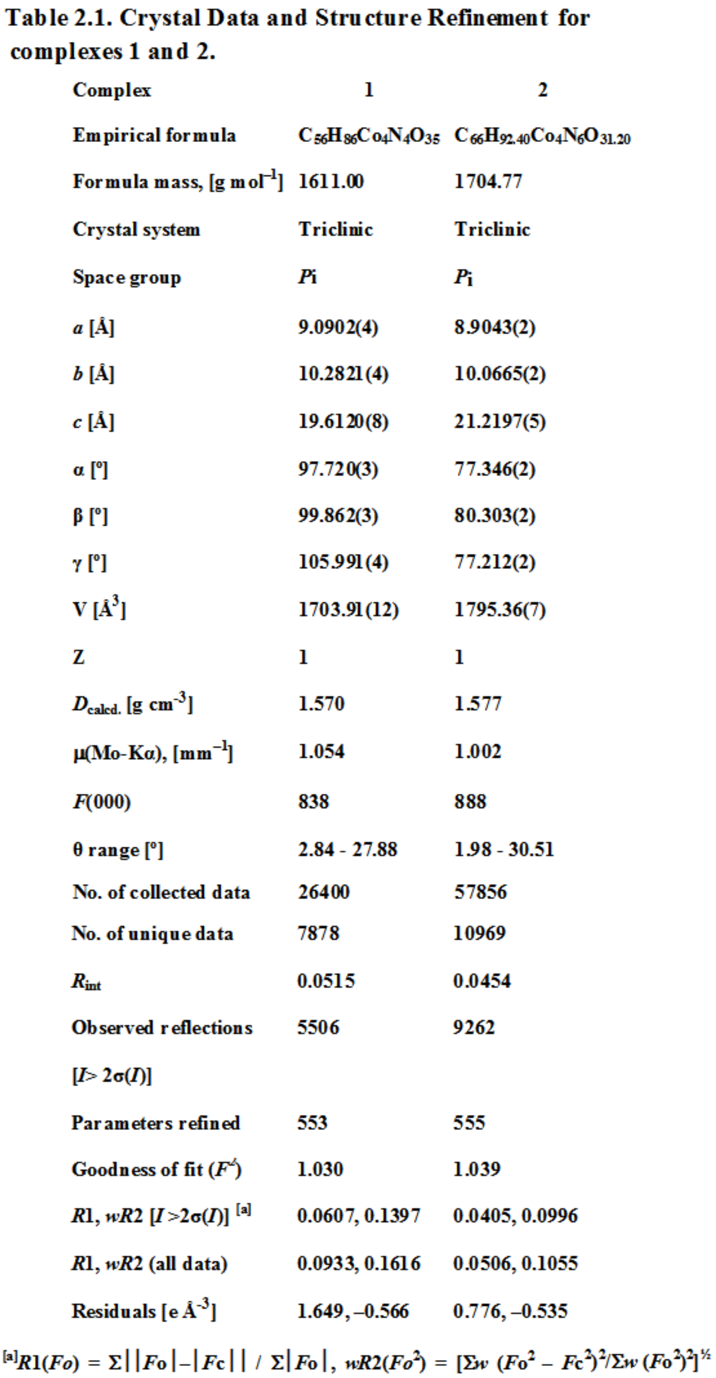

Table 2.1. Crystal Data and Structure Refinement for complexes 1 and 2.

Complex	1	2
Empirical formula	$C_{56}H_{86}Co_4N_4O_{35}$	$C_{66}H_{92.40}Co_4N_6O_{31.20}$
Formula mass, [g mol^{-1}]	1611.00	1704.77
Crystal system	Triclinic	Triclinic
Space group	*P*i	*P*i
a [Å]	9.0902(4)	8.9043(2)
b [Å]	10.2821(4)	10.0665(2)
c [Å]	19.6120(8)	21.2197(5)
α [°]	97.720(3)	77.346(2)
β [°]	99.862(3)	80.303(2)
γ [°]	105.991(4)	77.212(2)
V [Å^3]	1703.91(12)	1795.36(7)
Z	1	1
$D_{calcd.}$ [g cm^{-3}]	1.570	1.577
μ(Mo-K*α*), [mm^{-1}]	1.054	1.002
F(000)	838	888
θ range [°]	2.84 - 27.88	1.98 - 30.51
No. of collected data	26400	57856
No. of unique data	7878	10969
R_{int}	0.0515	0.0454
Observed reflections [$I > 2\sigma(I)$]	5506	9262
Parameters refined	553	555
Goodness of fit (F^2)	1.030	1.039
*R*1, *wR*2 [$I > 2\sigma(I)$] [a]	0.0607, 0.1397	0.0405, 0.0996
*R*1, *wR*2 (all data)	0.0933, 0.1616	0.0506, 0.1055
Residuals [e Å^{-3}]	1.649, –0.566	0.776, –0.535

[a] $R1(Fo) = \Sigma||Fo|-|Fc|| / \Sigma|Fo|$, $wR2(Fo^2) = [\Sigma w\ (Fo^2 - Fc^2)^2/\Sigma w\ (Fo^2)^2]^{½}$

2.2.4. Magnetic Measurements

Variable-temperature (2.0–300 K) dc magnetic susceptibility measurements under applied fields of 250 G ($T < 30$ K) and 0.5 T ($T \geq 30$ K) and field-dependent (0–5.0 T) magnetization measurements at low temperatures in the range 2.0–10.0 K were performed with a Quantum Design superconducting quantum interference device (SQUID) magnetometer. Variable-temperature (2.0–14.0 K) ac magnetic susceptibility measurements under ±4.0 G oscillating field at frequencies in the range 1.0–10.0 kHz were performed under different applied static fields in the range 0.0–2.5 kG with a Quantum Design physical property measurement system (PPMS). The magnetic susceptibility data were corrected for the diamagnetism of the constituent atoms and the sample holder. The dc and ac magnetic measurements were performed with powdered microcrystals (18.69 and 13.07 mg for **1** and **2**, respectively), and the samples were restrained with *n*-eicosane (27.84 and 28.47 mg for **1** and **2**, respectively) to avoid any field-induced torqueing.

2.2.5. Computational Details

As the magnetic coupling between Co^{II} ions through extended dicarboxylate ligands is negligible, all calculations were performed with the experimental geometries of the $\{Co^{II}Co^{III}\}$ units, that is, only one of the two Co^{II} ions was considered. Thus, all of the ligands of the $\{Co^{II}Co^{III}\}$ unit were fully taken into account, but the dicarboxylate bridging ligands were simplified in the distant region from the Co^{II} ion to gain efficiency without loss of accuracy. A view of the molecular models used in these calculations is shown in Figure 2.2. The parameters that determine the axial (D) and rhombic (E) zfs were estimated from calculations based on a second-order N-electron valence state perturbation theory (NEVPT2) applied on a wave function, which was previously obtained from a complete active space (CAS) calculation. These calculations were performed with the ORCA program version 3.0 [2.23] with the TZVP basis set proposed by Ahlrichs[2.24] and the auxiliary TZV/C Coulomb fitting basis sets.[2.25] The second-order contributions to the zfs from 10 quartet and 20 doublet excited states were generated from an active space with seven electrons in the d orbitals. The *g* tensor was calculated for the ground and excited Kramers pairs with multireference configuration interaction (MRCI) wave functions with a first-order perturbation theory on the SOC matrix.[2.26]

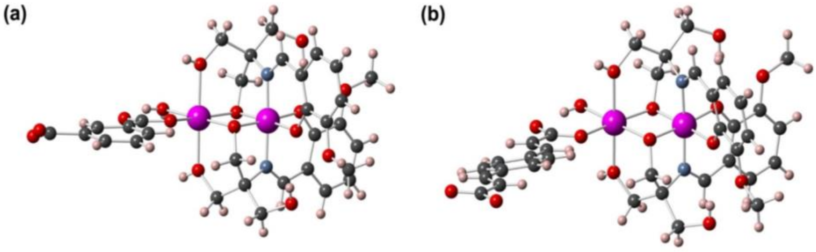

Figure 2.2. View of molecular models built from the experimental crystal structures of 1 (a) and 2 (b) and used in NEVPT2 calculations to evaluate the *zfs* parameters, *D* and *E*. Cobalt, nitrogen, oxygen, carbon and hydrogen atoms are displayed in magenta, light blue, red, grey and pink colours, respectively.

2.3. Results and discussion

2.3.1. Crystal-Structure Descriptions

The reaction of cobalt acetate with H_4L in methanol and in the presence of triethylamine and *m*-phthalic acid (molar ratio, cobalt acetate/H_4L/H_2phth = 1:1:1) leads to two ionic dinuclear complexes, a cationic $[Co_2(H_2L)_2(H_2O)_2]^+$ unit and an anionic $[Co_2(H_2L)_2(H_2O)(m\text{-phth})]^-$ species. A detail of the packing that occurs around a symmetry center and leads to positional disorder is shown in Figure 2.3. As described in the Experimental Section, a half occupancy has been assigned to the *m*-phth anion as well as to the coordinated aqua ligand O(2w) and lattice water molecules O(3w)–O(9w). The sixth coordination site of Co(2) is occupied by a carboxylate *m*-phth oxygen atom, and that of the symmetry-related Co(2′) atom is occupied by a water molecule; therefore the formulation for **1** is $[Co_2(H_2L)_2(H_2O)_2][Co_2(H_2L)_2(H_2O)(m\text{-phth})]\cdot 8(H_2O)$.

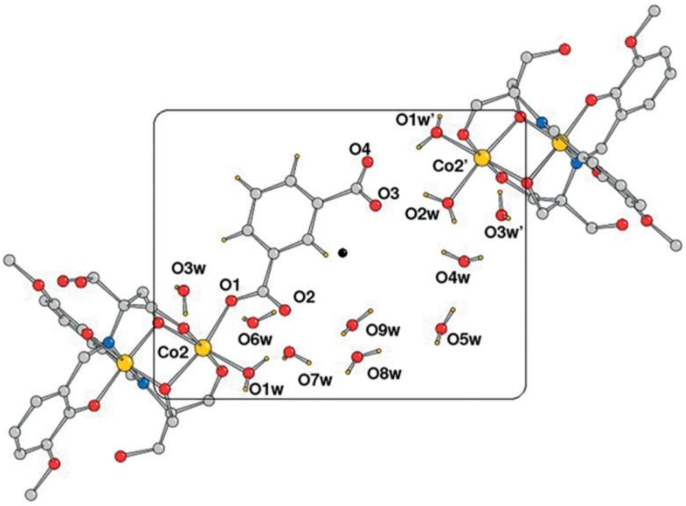

Figure 2.3. Crystal packing of 1: the *m*-phth anion, the coordinated aqua ligand O2w, and lattice water molecules O4w–O9w (all at half occupancy) share the same area owing to the crystallographic symmetry center represented by the black dot.

An ORTEP view of the anionic fragment is shown in Figure 2.4, and the *m*-phth anion acts as a monodentate ligand. The oxidation states of the cobalt centers are confirmed by consideration of the Co–O bond lengths and the total charge of the coordinated ligands. Co(1) has a +3 oxidation state and is chelated by two polydentate H_2L^{2-} Schiff base ligands through the phenoxido oxygen atoms O(1a/O1b), the imine nitrogen atoms N(1a/1b), and the deprotonated alcoholic –OH groups (O2a/2b). These chelating ligands are arranged such that the imine nitrogen donors are in *trans* positions, and the phenolato mean planes are almost normal to each other, as was found already for polynuclear cobalt complexes containing comparable fragments.[2.27]

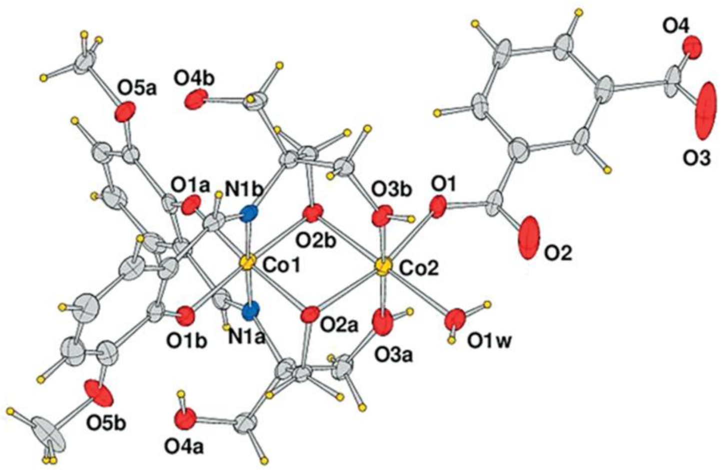

Figure 2.4. ORTEP drawing (40 % probability ellipsoids) of the $[Co_2(H_2L)_2(H_2O)\text{-}(m\text{-}phth)]^-$ anion of 1. The labels of the C atoms are omitted for clarity.

The Co(1)–N bond lengths are 1.887(3) and 1.889(3) Å, and the Co(1)–O bond lengths fall in the range 1.885(3)–1.915(2) Å. On the other hand, the divalent Co(2) ion has an O_6 chromophore environment and is coordinated by the bridging alkoxido oxygen atoms O(2a) and O(2b), the hydroxy groups O(3a) and O(3b), and a water molecule [O(1w)]. The sixth position is occupied by an additional aqua ligand [O(2w)] in the complex cation or by the *m*-phth carboxylate oxygen donor O(1) in its anionic counterpart. The Co(2)–O bond lengths are slightly longer and vary from 2.028(3) to 2.192(3) Å, but, owing to the disorder, the refinement led to Co(2)–O(2w)′ and Co(2)–O(1) bond lengths of 2.06(2) and 2.05(2) Å, respectively, with low accuracy.

The Co(2)–O bond lengths are significantly longer by 0.1–0.2 Å than those measured for Co(1), consistent with the designation of the oxidation states of +2 and +3 for Co(2) and Co(1), respectively. The alkoxido oxygen atoms O(2a) and O(2b) of the two H_2L ligands bridge the two cobalt centers, which have an intermetallic Co^{II}–Co^{III} distance of 2.9847(7) Å.

On the other hand, the reaction of cobalt acetate with H_4L in methanol in the presence of triethylamine and 1,4-benzenediacrylic acid (H_2ppda) (molar ratio, cobalt acetate/H_4L/ H_2ppda = 1:1:1) led to the formation of a centrosymmetric tetranuclear complex of formula $[Co_4(H_2L)_4(H_2O)_2(ppda)]\cdot 2(dmf)\cdot 3.2(H_2O)$ (**2**). The X-ray structural analysis of the compound revealed that it comprises a crystallographically independent dinuclear Co^{II}Co^{III} unit connected to a symmetry-related one by the phenylenediacrylate anion located on a center of symmetry. The molecular structure of **2** is illustrated in Figure 2.5, and selected bond lengths and angles are reported in Table 2.2. The metal atoms in the independent unit are six-coordinate with distorted octahedral geometries that show a close similarity to those of the anionic complex **1**. The intermetallic distance in the Co^{II}Co^{III} unit is 2.9654(3) Å (shorter than the value for **1** by 0.02 Å), and the Co(2) ions bridged by the ppda anion are separated by 15.225(1) Å. The same coordinating atom labels were assigned in **1** and **2**, and the data in Table 2.2 highlight the closeness of the geometric values in the two complexes. Owing to these similarities, we do not describe the structure in detail, and the Co–N and Co–O bond lengths are well within the ranges indicated previously for **1**, but the coordination bond angles in the present case indicate an octahedral geometry that is closer to the ideal arrangement.

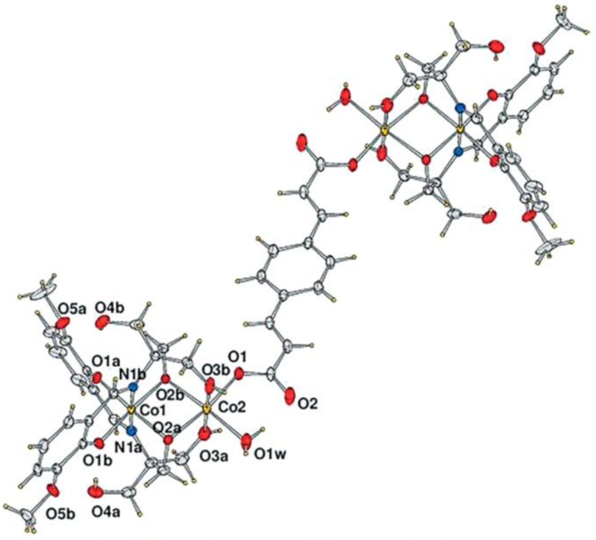

Figure 2.5. ORTEP drawing (50 % probability ellipsoids) of the centrosymmetric molecular structure of 2 (labels of C atoms omitted for clarity).

Table 2.2. Coordination bond lengths [Å] and angles [°] for 1 and 2.[a]

	1	2
Co(1)-N(1a)	1.889(3)	1.8861(15)
Co(1)-N(1b)	1.887(3)	1.8899(15)
Co(1)-O(1a)	1.885(3)	1.8749(12)
Co(1)-O(1b)	1.899(3)	1.9005(13)
Co(1)-O(2a)	1.915(2)	1.9123(12)
Co(1)-O(2b)	1.894(3)	1.8870(12)
Co(2)-O(1)	2.05(2)	2.0213(14)
Co(2)-O(2a)	2.028(3)	2.0379(13)
Co(2)-O(2b)	2.050(3)	2.0235(12)
Co(2)-O(3a)	2.192(3)	2.1971(14)
Co(2)-O(3b)	2.155(3)	2.1895(14)
Co(2)-O(1w)	2.078(3)	2.0904(15)
Co(2)-O(2w)'	2.06(2)	-
Co(1)-Co(2)	2.9847(7)	2.9654(3)
N(1a)-Co(1)-N(1b)	177.43(13)	176.69(6)
O(1a)-Co(1)-O(2a)	175.19(11)	176.35(5)
O(1b)-Co(1)-O(2b)	176.11(11)	175.52(6)
O(3a)-Co(2)-O(3b)	176.75(12)	177.72(6)
O(2b)-Co(2)-O(1w)	179.74(11)	173.69(6)
O(2a)-Co(2)-O(1)	162.4(4)	170.38(5)
O(2a)-Co(2)-O(2w)'	173.5(4)	-
Co(1)-O(2a)-Co(2)	98.36(11)	97.25(5)
Co(1)-O(2b)-Co(2)	98.30(11)	98.57(5)

[a] Symmetry code for O(2w)' in 1 = - x+1, - y+1, - z+1.

Notably, a rather strong intramolecular hydrogen bond occurs between the carboxylate oxygen atom O(2) and the adjacent coordinated water molecule O(1w) in both complexes [O•••O distances of 2.654(13) and 2.625(2) Å, in **1** and **2**, respectively, Figures 2.3 and 2.5] and reinforces the link of the carboxylate group to the dinuclear cobalt unit. However, the disorder of the water molecules observed in both crystals does not allow a detailed analysis of the H-bonding patterns. The volume of the lattice water molecules and dmf molecules in **2** accounts for 19 % of the unit cell volume, as derived by the program Platon.[2.28]

2.3.2. Magnetic Properties

The direct current (dc) magnetic properties of **1** and **2** in the form of the $\chi_{\mathrm{M}}T$ versus T plots [χ_{M} is the dc magnetic susceptibility per $(\mathrm{Co^{II}Co^{III}})_2$ unit] were investigated in detail (Figures 2.6 and 2.7). At room temperature, the $\chi_{\mathrm{M}}T$ values for **1** and **2** of 5.80 and 5.89 $\mathrm{cm^3mol^{-1}K}$, respectively, are within the range expected for two isolated high-spin d^7 $\mathrm{Co^{II}}$ (S = 3/2) ions with some orbital momentum contributions. As the temperature decreases, the $\chi_{\mathrm{M}}T$ value decreases continuously and reach 3.54 and 3.60 $\mathrm{cm^3mol^{-1}K}$ for **1** and **2**, respectively, at 2.0 K (Figures 2.6 and 2.7), and this reveals the occurrence of a significant spin-orbit coupling. On the other hand, these temperature dependences of the magnetic susceptibility confirm that the extended bridging ligands connecting the high-spin $\mathrm{Co^{II}}$ ions in **1** and **2** are not able to transmit a magnetic coupling strong enough to manifest its effects in the working temperature range, and the $\mathrm{Co^{II}}$ centres are considered to be entirely isolated. The magnetization data also support the presence of a spin-orbit coupling or *zfs*: (1) even at 2 K, the saturation magnetization values (4.30 and 4.26 $N\beta$ for **1** and **2**, Figures 2.6 and 2.7) are well below the expected value (Ms = 6.0 $N\beta$ for g = 2.0); and (2) the M versus H/T curves do not superimpose (Figures 2.8 and 2.9). However, the latter curves are very close and reveal systems with very small or large *zfs*. In the last case, which is usual for high-spin octahedral $\mathrm{Co^{II}}$ ions, the quartet ground state is split into two well-separated Kramer’s doublets, and practically only the Kramers doublet ground state is populated at low temperatures. Thus, changes in the temperature only cause tiny adjustments to the populations of the Kramer’s doublets and, in consequence, in the M versus H/T curves (Figures 2.8 and 2.9).

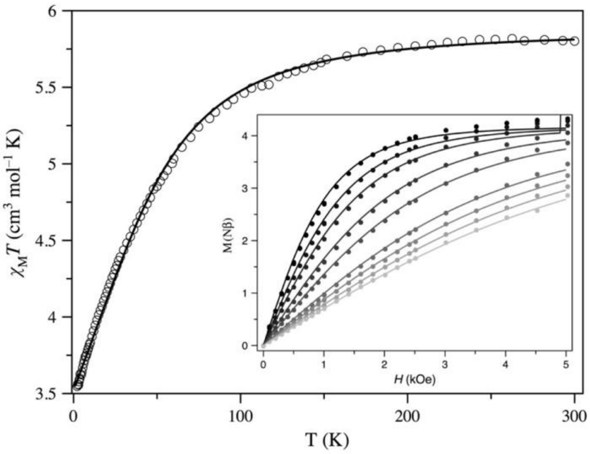

Figure 2.6. Thermal dependence of $\chi_M T$ of 1 under applied dc fields of 0.25 ($T < 30$ K) and 5.0 kG ($T \geq 30$ K): () experimental data; (–) best-fit curve (see text). The inset shows the dependence of *M* with *H* for 1 at 2.0, 2.5, 3.0, 4.0, 5.0, 7.0, 8.0, 9.0 and 10.0 K (from black to palest grey dots). The solid lines are the best-fit curves (see text).

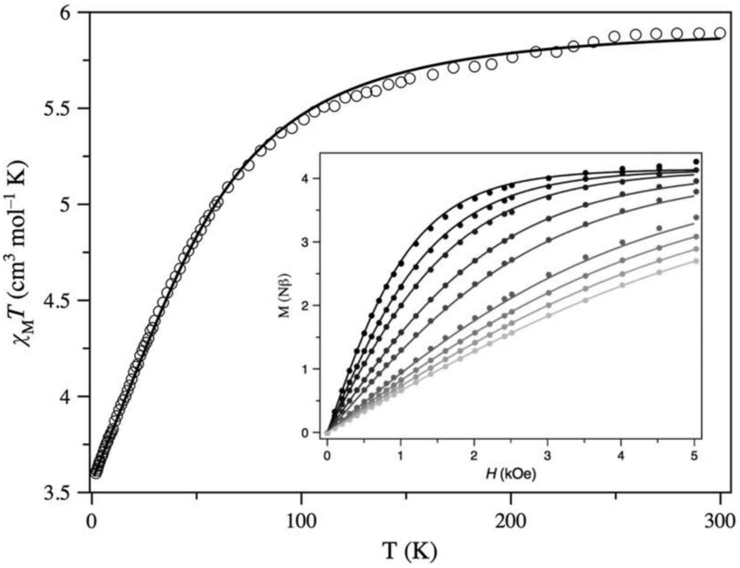

Figure 2.7. Thermal dependence of $\chi_M T$ of 2 under applied dc fields of 0.25 ($T < 30$ K) and 5.0 kG ($T \geq 30$ K): () experimental data; (–) best-fit curve (see text). The inset shows the dependence of *M* with *H* for 1 at 2.0, 2.5, 3.0, 4.0, 5.0, 7.0, 8.0, 9.0 and 10.0 K (from black to palest grey dots). The solid lines are the best-fit curves (see text).

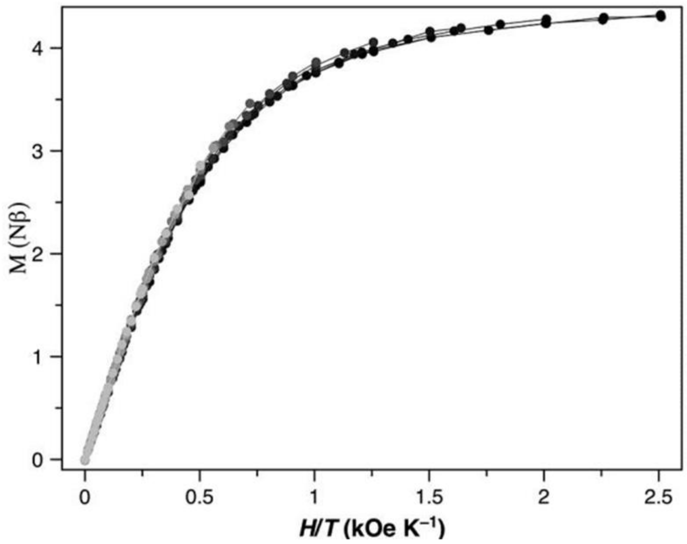

Figure 2.8. Dependence of *M* with *H*/*T* of 1 in a temperature range starting at 2.0, 2.5, 3.0, 4.0, 5.0, 7.0, 8.0, 9.0 and 10.0 K (from black to palest grey dots).

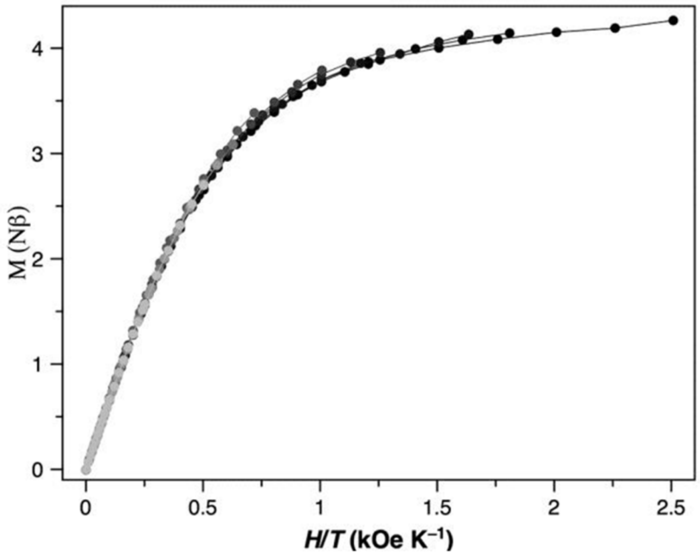

Figure 2.9. Dependence of *M* with *H*/*T* of 2 in a temperature range starting at 2.0, 2.5, 3.0, 4.0, 5.0, 7.0, 8.0, 9.0 and 10.0 K (from black to palest grey dots).

Although the magnetic susceptibility data should be analyzed with a model of a first-order spin-orbit coupling for significant SOC, a spin Hamiltonian corresponding to an isolated S = 3/2 with large g-factors and zfs parameters can be used. In this case, the spin Hamiltonian takes the form: $\mathrm{H} = D[S_z^2+S(S+1)/3] + E(S_x^2+S_y^2) + \beta Hg(S_x+S_y+S_z)$, in which the axial and rhombic distortions of the tetragonally distorted high-spin d^7 $\mathrm{Co^{II}}$ ion are taken into account through the D and E parameters, respectively. Although the E parameter cannot be evaluated unambiguously from magnetic susceptibility data, the E and g parameters are strongly correlated in the simulation of the magnetization data. However, these problems can be solved if the magnetic susceptibility and magnetization data are analyzed in unison. Thus, the magnetic susceptibility data determines the value of the *g*-factor and, hence, the magnetization allows a good estimation of the rhombic anisotropy value from the determined *g* value. However, the huge *zfs* leads to a collapse of the *M* versus *H*/*T* curves that represents a major constraint to the achievement of a good estimation of the *D* and *E* parameters. Thus, we independently analyzed the thermal dependences of the magnetic susceptibility and the magnetization. The agreement factor (*F*) can be defined as $\sum[(P)_{exp} - (P)_{calcd}]^2/\sum[(P)_{exp}]^2$, in which P is the physical property under study. A minimum value of *F* for the magnetic susceptibility is reached with the following values: $g = 2.501(3)$ and $|D| = 54.7(7)\ \mathrm{cm}^{-1}$ with $F = 3.6\times 10^{-5}$ for **1** and $g = 2.515(2)$ and $|D| = 60.8(6)\ \mathrm{cm}^{-1}$ with $F = 2.5\times 10^{-5}$ for **2**. The theoretical curves match the experimental data well in the whole temperature range (solid lines in Figures 2.6 and 2.7). Hence, the assumption that the $\mathrm{Co^{II}}$ ions are magnetically isolated is validated. In $\mathrm{Co^{II}}$ SIMs, these large values of the axial *zfs* are typical, but both negative and positive values have been reported.[2.11a-2.11c,2.18] On the other hand, the large axial *zfs* allows simulation of the magnetization data with a spin model that takes into account only the ground Kramer's doublet as an effective S = ½ spin moment. In this approach, the magnetic anisotropy is transferred to the *g* tensor, that is, three different components should be considered. Usually, only the parallel ($g_{\|}$) and perpendicular components ($g_{\perp}$) are contemplated. This model is summarized in the spin Hamiltonian: $\mathbf{H} = g_{\perp}\beta H_x S_x + g_{\perp}\beta H_y S_y + g_{\|}\beta H_z S_z$. Thus, the best fit of the magnetization data provides the following results: $g_{\|} = 7.519(10)$ and $g_{\perp} = 1.901(9)$ with $F = 3.0 \times 10^{-4}$ for **1**; and $g_{\|} = 7.349(8)$ and $g_{\perp} = 1.950(7)$ with $F = 3.6 \times 10^{-4}$ for **2** (solid lines in Figures 2.6 and 2.7). These values, especially the large values of $g_{\|}$, are typical for octahedral $\mathrm{Co^{II}}$ ions with negative *D* values.

On the other hand, these values of the *D* and *E*/*D* parameters agree with those found from NEVPT2 calculations. Owing to the coexistence of cationic (**1**$^+$) and anionic (**1**$^-$) units in **1**, NEVPT2 calculations were performed for both species to estimate the zfs parameters. In all used models, Co^{II} and Co^{III} ions are present, and the unique metal ion that shows a spin density (ϱ) that corresponds to a partially delocalized high-spin d^7 electronic configuration is that assigned to a Co^{II} ion from the crystal structure [ϱ(Co) = 2.89 e]. Although *D* and *E*/*D* take similar values for **1**$^-$ (D = –95.8 cm^{-1} and E/D = 0.216) and **2** (D = –101.9 cm^{-1} and E/D = 0.234), these values are lower for **1**$^+$ (D = –62.4 cm^{-1} and E/D = 0.219). The values obtained from a second-order perturbative approach are qualitatively similar to those reached for an effective Hamiltonian (D = +55.9, –70.4 and –73.9 cm^{-1}; E/D = 0.294, 0.328 and 0.331 for **1**$^+$, **1**$^-$ and **2**, respectively) but are closer to those found from the magnetometry. However, in our experience, the effective Hamiltonian approach usually overestimates the rhombicity in the zfs, and the *E*/*D* ratio is close to its maximum value (1/3); thus, the meaning of the sign of *D* is lost. Mainly, these results confirm the negative sign of *D* suggested from the experimental magnetization data. According to these calculations, the second-order spin–orbit coupling is the main contribution to the *D* parameter, and the contribution of the spin–spin coupling is negligible compared to the former one. As the two first quartet excited states are much closer to the quartet ground state (786 and 1519 cm^{-1} in **1**$^-$) than the other quartet and doublet excited states, the *D* value is largely given by the contribution from these two excited states (–108.7 and +19.4 cm^{-1}, respectively). Although the Co^{II} ions in **1**$^-$ and **2** present the same coordination environment, the calculations shows that **2** exhibits a higher zfs, which is probably related to a larger distortion of the octahedral coordination sphere, as is supported by a major value of *E*/*D*. This provokes the first two excited quartet states to be slightly closer to the ground state (776 and 1449 cm^{-1}) than those in **1**$^-$ (786 and 1519 cm^{-1}), and they interact more strongly with it to lead to major contributions to the *D* parameter in **2**

(–118.4 and +22.8 cm^{-1}). Shape measurements were performed for $\mathbf{1}^{+}$, $\mathbf{1}^{-}$, and **2** to check the involvement of structural distortions on the different zfs suggested for $\mathbf{1}^{+}$. Previous theoretical studies indicated that octahedral geometries favor positive *D* parameters, but trigonal-prismatic coordination spheres provide negative *D* factors.[2.29] The shape measurements for our three complexes suggest that they are very similar with coordination spheres that are close octahedral [S = 18.4 ($\mathbf{1}^{+}$), 21.1 ($\mathbf{1}^{-}$), and 17.0 (**2**); here, S is the degree of conversion between an octahedron and a trigonal prism and takes values of 0.0 and 100 for an ideal octahedron and a trigonal prism].[2.30] However, they are distorted and deviated from the path that connects an octahedron and a trigonal prism; these deviations are also similar for the three species (δ = 11.3, 7.6, and 9.4 for $\mathbf{1}^{+}$, $\mathbf{1}^{-}$ and **2**, respectively). Therefore, the structural parameters cannot explain the different calculated axial zfs for $\mathbf{1}^{+}$ and the similar values $\mathbf{1}^{-}$ and **2**. On the other hand, the negative *D* values for the three units do not agree with an octahedral geometry.[2.29] High rhombicity, as is proposed for **1** and **2**, can inverse the sign of *D* or remove its physical meaning. Nevertheless, the zfs must be associated with electronic effects rather than structural factors, although they can be coincident in some cases, particularly in theoretical studies in which only structural distortions are applied in a specific model. In other situations, the ligands forming the coordination sphere can display different electronic structures, but geometric factors that influence the zfs play only a minor role. In the present case, the coordination spheres of $\mathbf{1}^{-}$ and **2** are similar, but a neutral water molecule replaces one charged carboxylate group in $\mathbf{1}^{+}$ and provokes an apparent change in the electronic structure of this last complex despite the insignificant structural change. This causes the similar *D* values for $\mathbf{1}^{-}$ and **2**, and the found difference can be associated only with structural features. However, this is not the case for $\mathbf{1}^{+}$, for which the change of the electronic state through the coordination of the water molecule shifts the first excited quartet (874 cm^{-1}), which is the main contributor to the axial zfs in octahedral cobalt(II) complexes, and decreases its input drastically. On the other hand, as these two excited quartet states contribute in opposite ways, the control of the symmetry of the electronic distribution allows the stabilization of one or other excited state and, hence, a positive or negative D value can be obtained. Additionally, from these calculations, an estimation of the three components of the g factor gave g_1 = 1.719, g_2 = 2.607 ($g_\perp$ = 2.208), and g_3 = g_z = 7.307 for $\mathbf{1}^+$; g_1 = 1.517, g_2 = 2.350 ($g_\perp$ = 1.978), and g_3 = g_z= 7.771 for $\mathbf{1}^-$; and g_1 = 1.510, g_2 = 2.392 ($g_\perp$ = 2.000), and g_3 = g_z = 7.845 for **2**, and these values agree with those previously obtained from the magnetization data.

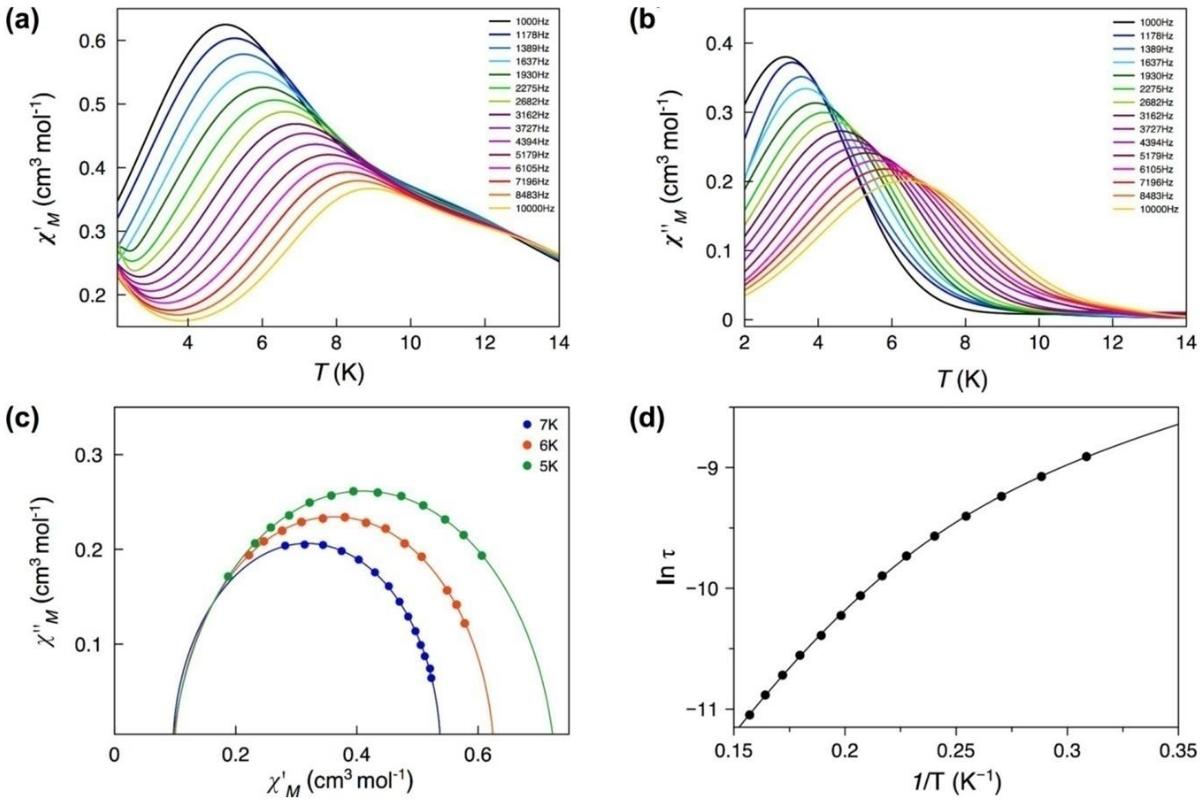

Figure 2.10. Temperature dependence of (a) χ_M' and (b) χ_M'' (b) of 1 in a dc applied static field of 1.0 kG and under ±4.0 G oscillating field at frequencies in the range 1.0–10 kHz. (c) The Cole–Cole plot at 5.0–7.0 K and (d) the Arrhenius plot in the high-temperature region for an applied static field of 1.0 kG.

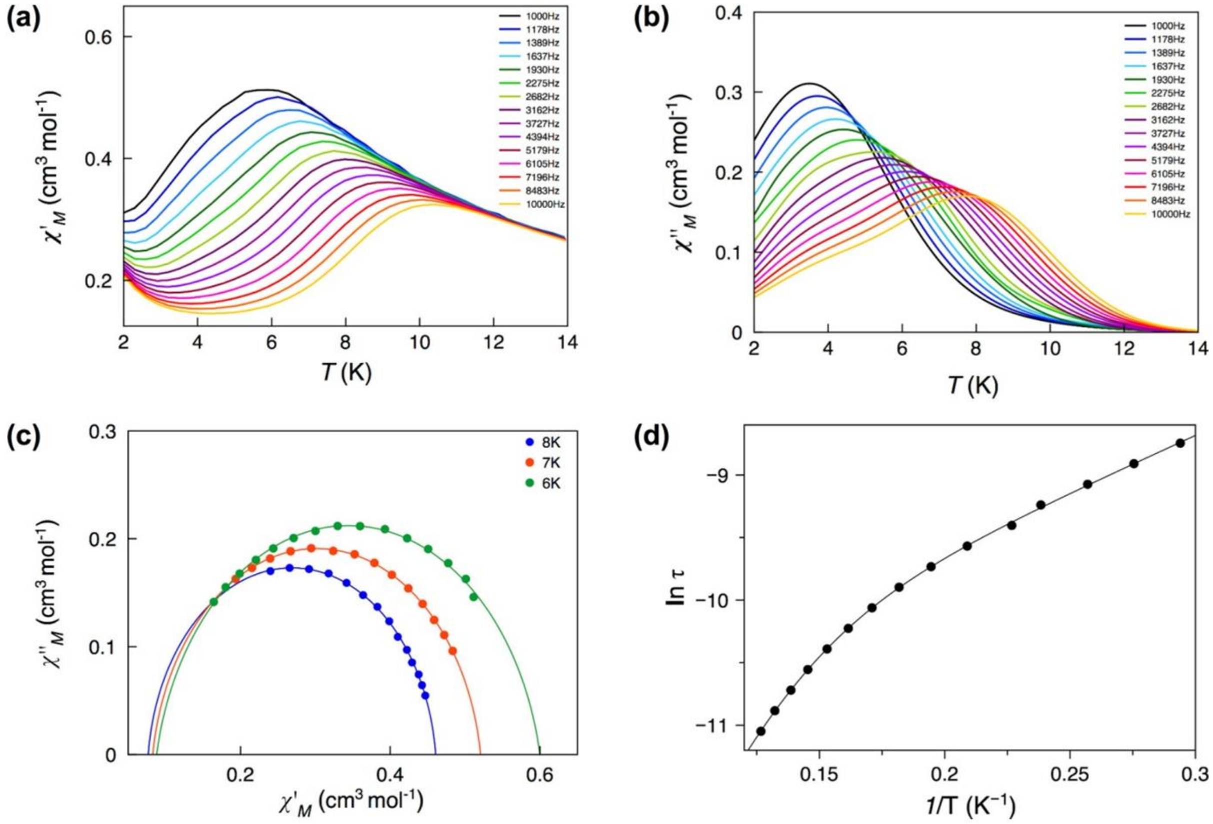

Figure 2.11. Temperature dependence of (a) χ_M' and (b) χ_M'' (b) of 2 in a dc applied static field of 1.0 kG and under ±4.0 G oscillating field at frequencies in the range 1.0–10 kHz. (c) The Cole– Cole plot at 5.0–7.0 K and (d) the Arrhenius plot in the high-temperature region for an applied static field of 1.0 kG.

The alternating current (ac) magnetic susceptibility of **1** and **2** in the form of the χ_M' and χ_M'' versus T plots [χ_M' and χ_M'' are the in-phase and out-of-phase ac magnetic susceptibilities per $(Co^{II}Co^{III})_2$ unit] were measured in different applied static fields in the range 0.0–2.5 kG (Figures 2.10, 2.11, 2.12-2.15). In zero dc magnetic field, no χ_M'' signals can be observed for **1** and **2**, even for the highest frequency used (ν = 10 kHz), and this suggests that fast zero-field quantum tunneling relaxation of the magnetization occurs. However, if a small static dc field of 500 G is applied, strong frequency-dependent maxima appear in both χ_M' and χ_M'' below 10 K (Figures 2.12 and 2.14) in both cases. Additional ac measurements for **1** and **2** under higher applied dc fields of 1000 and 2500 G are shown in (Figures 2.10, 2.11, 2.13 and 2.15), and the same single strong frequency-dependent χ_M'' maxima are observed below 10 K. Relaxation times for **1** and **2** could be calculated from the maximum of χ_M'' at a given frequency ($\tau = 1/2\pi\nu$). At higher temperatures and for all applied static DC magnetic fields, these follow the Arrhenius law and are characteristic of a thermally activated or Orbach mechanism (Figures 2.10d, 2.11d and 2.12d-2.15d), which is determined for the first pre-exponential factor (τ_0) and activation energy (E_a). However, in all cases, a deviation of the Arrhenius law at lower temperatures is observed, and this is a definite indication of the presence of another additional relaxation mechanism. Among the candidates for this are quantum tunneling, direct relaxation, and Raman relaxation mechanisms. The best simulation of the thermal dependence of the relaxation times was obtained for only the Orbach and Raman mechanisms through the $\tau^{-1} = \tau_0^{-1}\exp(-E_{a1}/k_BT) + AT^n$ relation. The values of first pre-exponential factor (τ_0) and activation energy (E_a) for **1** and **2** are consistent with those found for previously reported octahedral cobalt(II) SIMs (Tables 2.3 and 2.4).[2.11c] On the other hand, it is notable that, the Raman and direct mechanisms are expressed in a similar way for a particular applied magnetic field, and only the value of n changes from unity for the latter to larger values for the former, usually n = 7 and 9 for non-Kramers and Kramers ions, respectively. Lower values of n are possible if phonons are considered. Thus, although a direct mechanism seems to be present in **2**, a relaxation mechanism through a Raman process that takes into account phonons could be more appropriate in **1** (Tables 2.3 and 2.4).

Table 2.3. Selected ac magnetic data for 1 at different dc applied fields

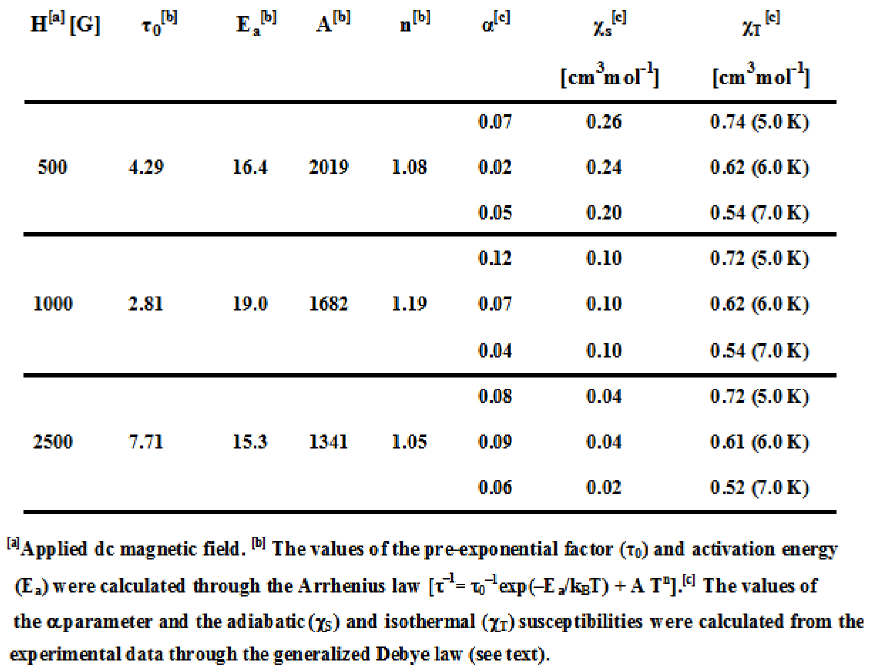

$H^{[a]}$ [G]	$\tau_0^{[b]}$	$E_a^{[b]}$	$A^{[b]}$	$n^{[b]}$	$\alpha^{[c]}$	$\chi_S^{[c]}$ [cm^3mol^{-1}]	$\chi_T^{[c]}$ [cm^3mol^{-1}]
500	4.29	16.4	2019	1.08	0.07	0.26	0.74 (5.0 K)
					0.02	0.24	0.62 (6.0 K)
					0.05	0.20	0.54 (7.0 K)
1000	2.81	19.0	1682	1.19	0.12	0.10	0.72 (5.0 K)
					0.07	0.10	0.62 (6.0 K)
					0.04	0.10	0.54 (7.0 K)
2500	7.71	15.3	1341	1.05	0.08	0.04	0.72 (5.0 K)
					0.09	0.04	0.61 (6.0 K)
					0.06	0.02	0.52 (7.0 K)

[a]Applied dc magnetic field. [b] The values of the pre-exponential factor (τ_0) and activation energy (E_a) were calculated through the Arrhenius law [$\tau^{-1} = \tau_0^{-1}\exp(-E_a/k_BT) + A\,T^n$].[c] The values of the α parameter and the adiabatic (χ_S) and isothermal (χ_T) susceptibilities were calculated from the experimental data through the generalized Debye law (see text).

Table 2.4. Selected ac magnetic data for 2 at different dc applied fields

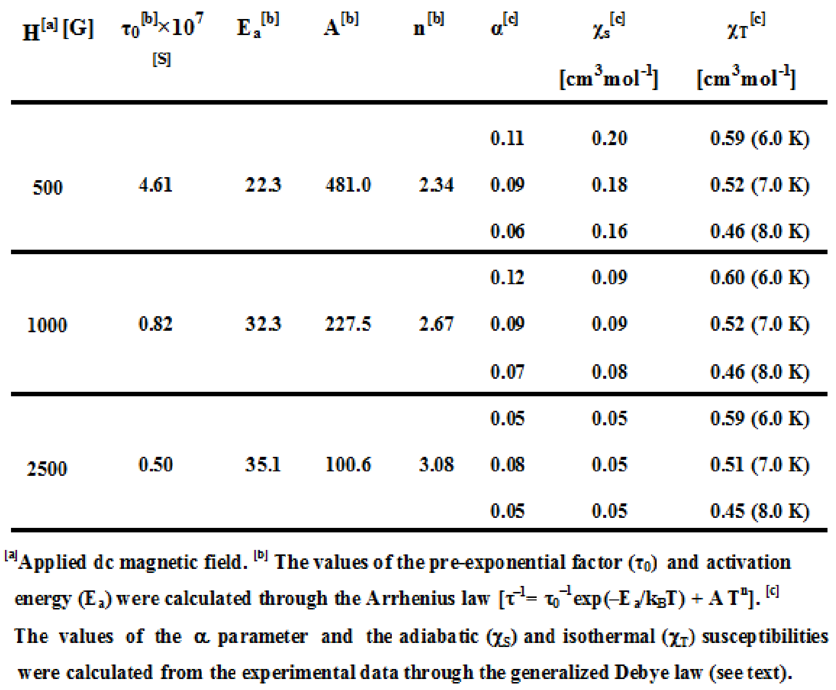

$H^{[a]}$ [G]	$\tau_0^{[b]}\times10^7$ [S]	$E_a^{[b]}$	$A^{[b]}$	$n^{[b]}$	$\alpha^{[c]}$	$\chi_S^{[c]}$ [cm^3mol^{-1}]	$\chi_T^{[c]}$ [cm^3mol^{-1}]
500	4.61	22.3	481.0	2.34	0.11	0.20	0.59 (6.0 K)
					0.09	0.18	0.52 (7.0 K)
					0.06	0.16	0.46 (8.0 K)
1000	0.82	32.3	227.5	2.67	0.12	0.09	0.60 (6.0 K)
					0.09	0.09	0.52 (7.0 K)
					0.07	0.08	0.46 (8.0 K)
2500	0.50	35.1	100.6	3.08	0.05	0.05	0.59 (6.0 K)
					0.08	0.05	0.51 (7.0 K)
					0.05	0.05	0.45 (8.0 K)

[a]Applied dc magnetic field. [b] The values of the pre-exponential factor (τ_0) and activation energy (E_a) were calculated through the Arrhenius law [$\tau^{-1} = \tau_0^{-1}\exp(-E_a/k_BT) + A\,T^n$]. [c] The values of the α parameter and the adiabatic (χ_S) and isothermal (χ_T) susceptibilities were calculated from the experimental data through the generalized Debye law (see text).

However, we would like to note that different sets of values for the parameters associated with the Orbach and Raman processes, as well as the consideration of quantum tunneling, were able to reproduce the thermal dependence of the relaxation time. Among these sets, it can be outlined that an energy barrier of close to 100 cm^{-1} is close to that provided by the *D* parameter. However, the Raman *A* and *n* parameters unexpectedly always depend on the applied static magnetic field. The *n* parameter seems to be independent of the magnetic field only for **1**, for which it takes a value close to the unity as a direct relaxation process is presumed. In our experience of other families of cobalt(II) complexes, additional relaxation processes together with an Orbach mechanism do not provide satisfactory results because the simulations are not good enough or the dependence with the applied magnetic field is not that expected. In such cases, the inclusion of a second Orbach mechanism gives a good answer.[2.31] For **1** and **2**, this can also be applied to provide values for the energy barriers and pre-exponential factors similar to others reported previously (Table 2.5). However, at lower temperature, for which we have relaxation times for all magnetic fields used (3.8 K), it seems that there is a correlation between τ and *H*; therefore, a direct relaxation process cannot be discarded.

Table 2.5. Selected ac magnetic data for 1 and 2 at different dc applied fields

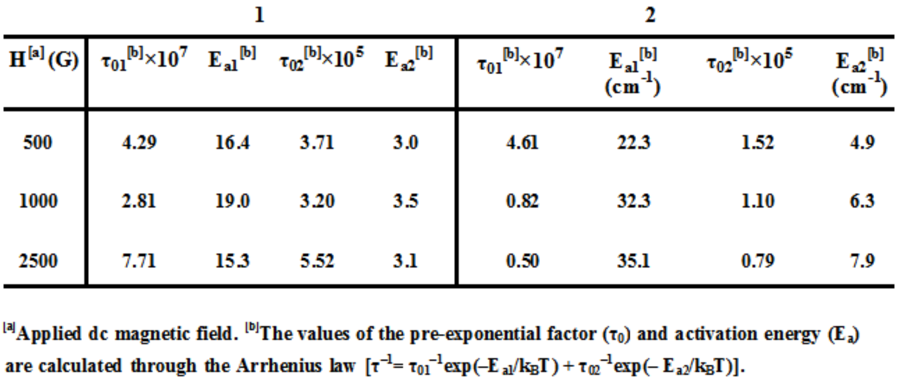

	1				2			
H[a] (G)	τ_{01}[b]$\times 10^7$	E_{a1}[b]	τ_{02}[b]$\times 10^5$	E_{a2}[b]	τ_{01}[b]$\times 10^7$	E_{a1}[b] (cm^{-1})	τ_{02}[b]$\times 10^5$	E_{a2}[b] (cm^{-1})
500	4.29	16.4	3.71	3.0	4.61	22.3	1.52	4.9
1000	2.81	19.0	3.20	3.5	0.82	32.3	1.10	6.3
2500	7.71	15.3	5.52	3.1	0.50	35.1	0.79	7.9

[a]Applied dc magnetic field. [b]The values of the pre-exponential factor (τ_0) and activation energy (E_a) are calculated through the Arrhenius law [$\tau^{-1} = \tau_{01}^{-1}\exp(-E_{a1}/k_BT) + \tau_{02}^{-1}\exp(-E_{a2}/k_BT)$].

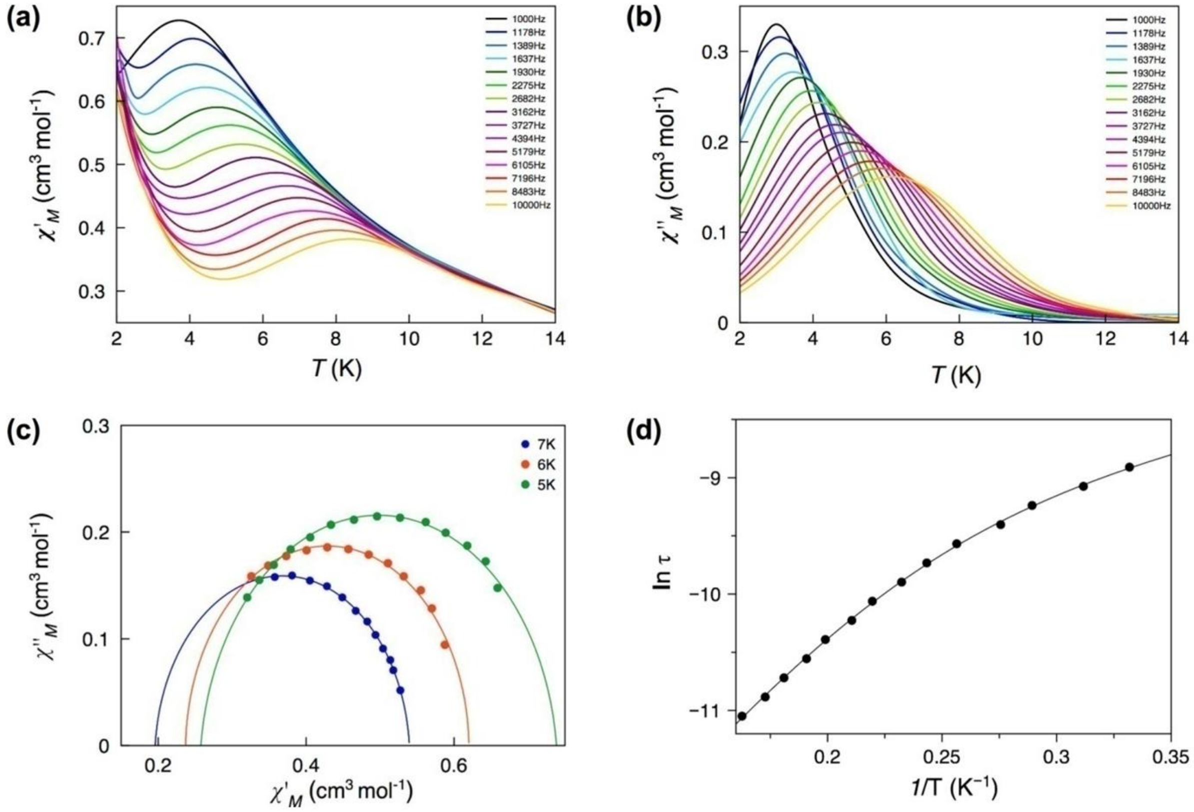

Figure 2.12. Temperature dependence of χ_M‘ (a) and χ_M“ (b) of 1 in a dc applied static field of 0.5 kG and under ±4.0 G oscillating field at frequencies in the range of 1.0–10 kHz. The Cole-Cole plot (c) at 5.0–7.0 K and the Arrhenius plot in the high temperature region (d) for an applied static field of 0.5 kG.

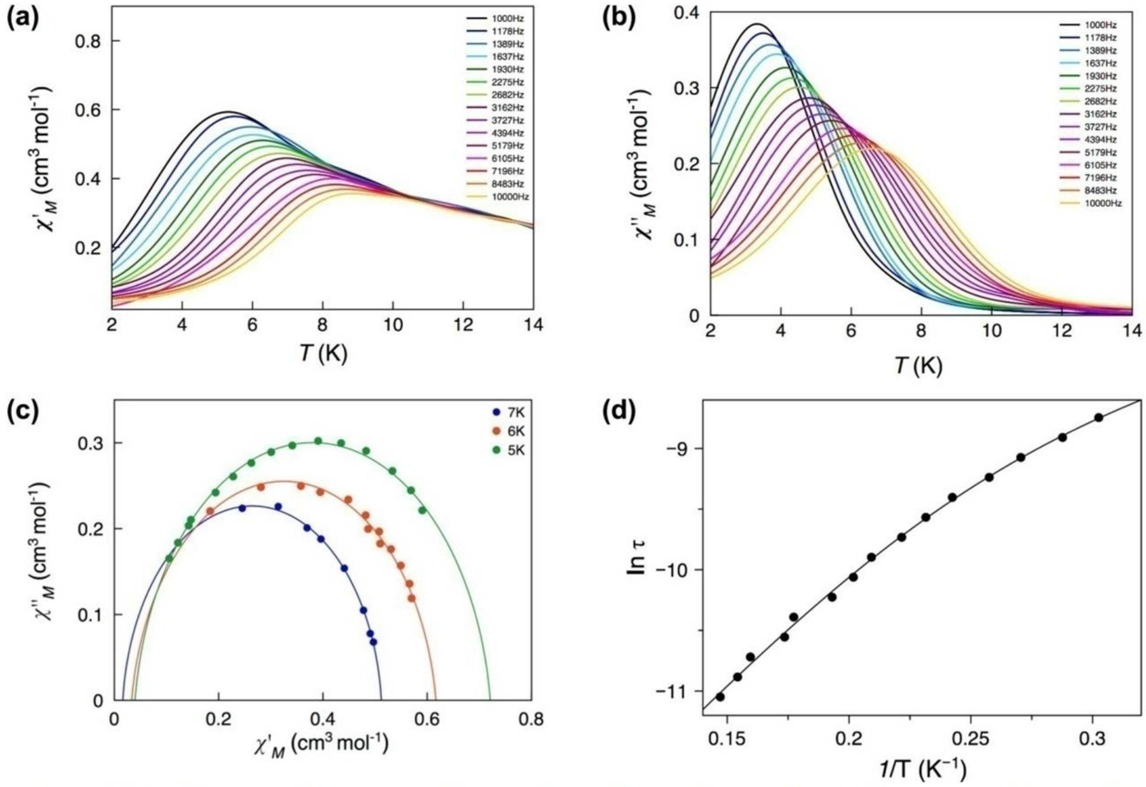

Figure 2.13. Temperature dependence of χ_M‘ (a) and χ_M“ (b) of 1 in a dc applied static field of 2.5 kG and under ±4.0 G oscillating field at frequencies in the range of 1.0–10 kHz. The Cole-Cole plot (c) at 5.0–7.0 K and the Arrhenius plot in the high temperature region (d) for an applied static field of 2.5 kG.

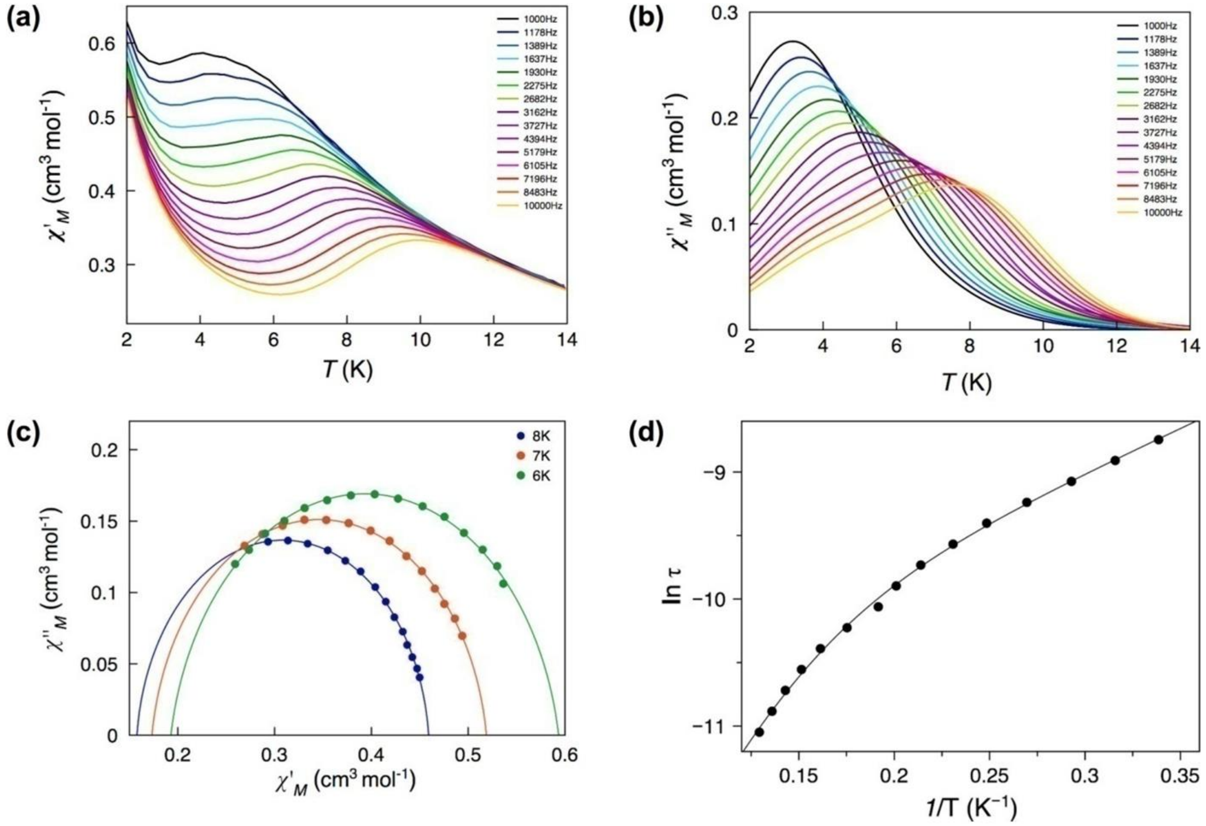

Figure 2.14. Temperature dependence of χ_M' (a) and χ_M" (b) of 2 in a dc applied static field of 0.5 kG and under ±4.0 G oscillating field at frequencies in the range of 1.0–10 kHz. The Cole-Cole plot (c) at 6.0–8.0 K and the Arrhenius plot in the high temperature region (d) for an applied static field of 0.5 kG.

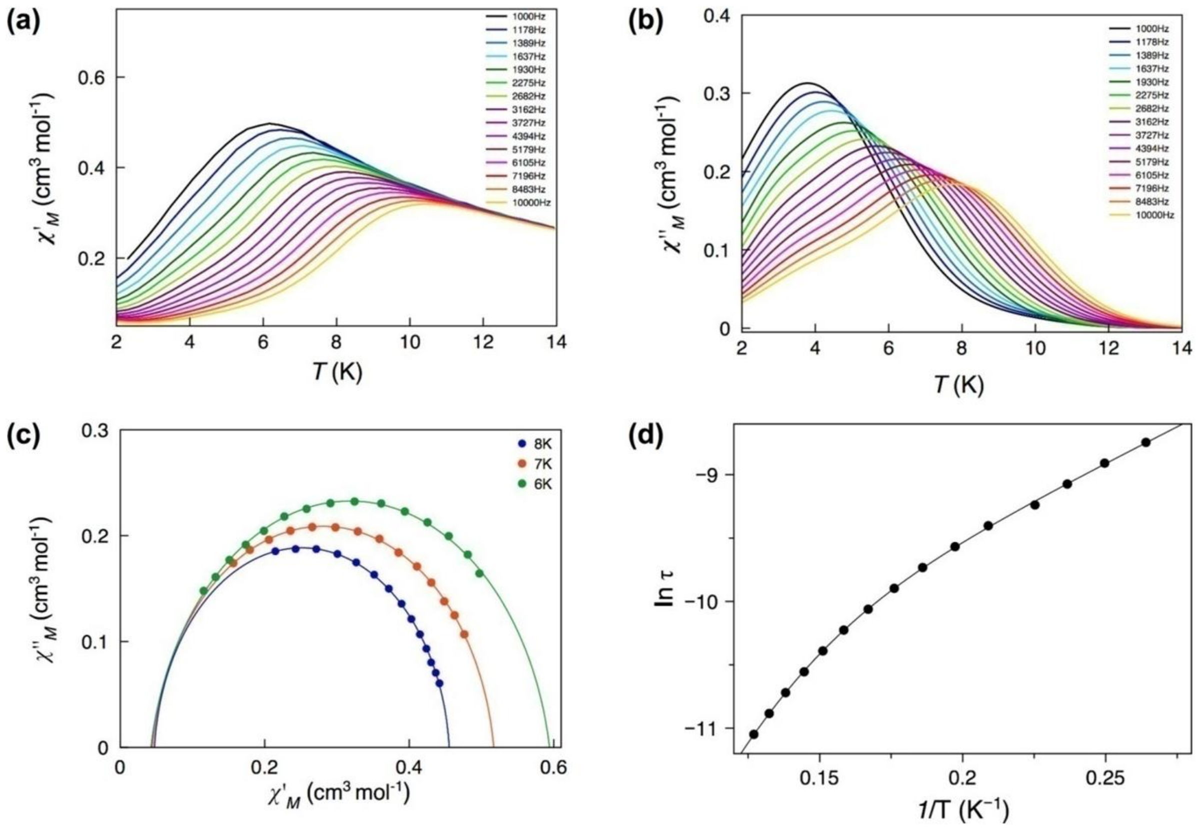

Figure 2.15. Temperature dependence of χ_M' (a) and χ_M'' (b) of 2 in a dc applied static field of 2.5 kG and under ±4.0 G oscillating field at frequencies in the range of 1.0–10 kHz. The Cole-Cole plot (c) at 6.0–8.0 K and the Arrhenius plot in the high temperature region (d) for an applied static field of 2.5 kG.

It is unclear which unit (cationic or anionic) behaves as a SIM in **1** or even if both do. On the basis of the resemblance observed particularly in the structural and electronic features between **1**$^-$ and **2** as well as the SIM behavior (energy barrier and relaxation times) reported for **1** and **2**, it is only natural to think that the anionic species **1**$^-$ is the unique unit in **1** that behaves as a SIM. Nevertheless, we cannot guarantee that the cationic unit **1**$^+$ does not show this particular behavior even it is the only form of the three complexes studied here that reveals a positive D value calculated from the effective Hamiltonian. On the other hand, for octahedral cobalt(II) complexes, it is very usual that the energy gap between the ground and first excited Kramers doublet is much larger than that suggested by the energy barrier obtained from the dynamic studies of the magnetization. In such cases, some authors propose that an extra energy contribution from a network relaxation through a phonon can decrease the energy that is necessary to overcome the barrier imposed by the zfs. The energy of these phonons depends directly on how the molecules are organized in the network and the strength and nature of the contacts between them. As the structural networks of **1** and **2** are very different, it is not possible to establish a direct correlation between the energy barriers and *D* values.

The Cole–Cole plots for **1** at 6.0–8.0 K and **2** at 5.0–7.0 K under different applied dc fields of 500, 1000, and 2500 G gave almost perfect semicircles, which could be fitted by the generalized Debye model[2.32] (solid lines in Figures 2.10c, 2.11c, and 2.12c–2.15c). The calculated low values of the α parameter at the different applied dc fields (α = 0.02–0.12, Table 2.3) support a single relaxation process and, thus, spin-glass behavior[2.33] can be discarded ($\alpha = 0$ for a Debye model) for both compounds. We could consider that **1** with two different cobalt(II) complexes should present a larger α value than **2** with one unique cobalt(II) unit. However, we have seen in the past that metal complexes both at the molecular level and in the bulk solid can display a relatively wide range of *D* values at low temperatures (5 or 10 K) because of the geometrical changes that occur at these temperatures. Briefly, at low temperatures, the complexes are still in motion and show a Gaussian distribution of the geometries and zfs parameters, and this is probably the cause of the presence of a distribution of relaxation processes and, therefore, a nonzero α value.[2.34] The amplitude of these distributions depends on the molecular vibrational frequencies but also on the nature and strength of the intermolecular contacts in the solid. It is not easy to establish an order of the α values for **1** and **2** because the crystal structures of **1** and **2** are relatively different.

2.3.3. IR spectral results of H_4L, complex 1 and 2

The IR spectrum of complex **1** and **2** (Figure 2.16) exhibits a strong broad band in the region 3200-3600 cm^{-1} is due to the ν(O-H) stretching vibration of free hydroxyl group of ligand. The bands at 2982 cm^{-1} and 2983 cm^{-1} for complex **1** and **2** respectively, corresponds to the aromatic ν(C-H) stretching vibrations and aliphatic ν(C-H) stretching vibrations for both complexes appears at 2946 cm^{-1}. On the other hand the bands are at 1171cm^{-1} and 1138 cm^{-1} for complex **1**, corresponding to ν(O-CH$_3$) stretching vibrations and for complex **2** these are at 1170 cm^{-1} and 1138 cm^{-1}. The appearance of a strong and sharp peak at 1639 cm^{-1} for **1** and 1642 cm^{-1} for **2** indicates the presence of unidentate bridging mode of carboxylate.

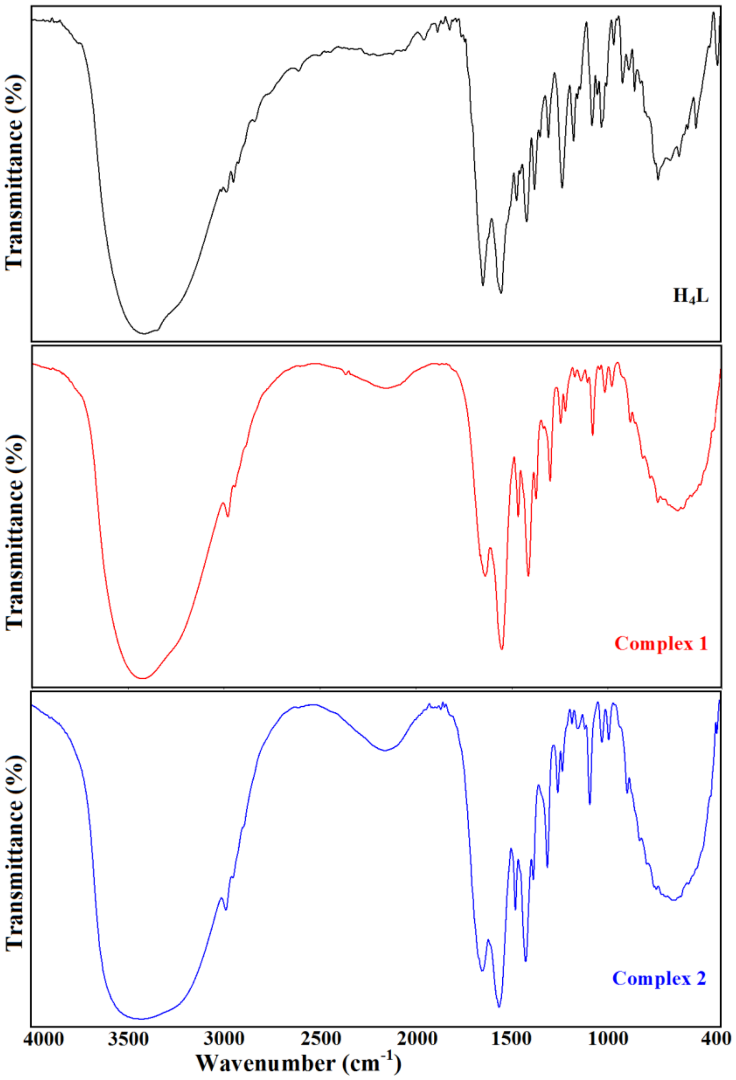

Figure 2.16. IR spectra of H$_4$L, 1 and 2.

2.3.4. Electronic absorption spectral results of H$_4$L, complexes 1 and 2

The electronic spectra of H$_4$L and complexes **1-2** were recorded in methanol (Figure 2.17). The spectrum of H$_4$L shows significant transitions at 202 nm (ε ~ 6.77×10^4 liter mole^{-1} cm^{-1}), 241 nm (ε ~ 5.56×10^4 liter mole^{-1} cm^{-1}), 293 nm (ε ~ 4.15×10^4 liter mole^{-1} cm^{-1}) and 420 nm (ε ~ 1.77×10^4 liter $mole^{-1}cm^{-1}$). On the other hand for complex **1** significant transitions are at 250 nm (ε ~ 3.13×10^4 liter $mole^{-1}$ cm^{-1}), 313 nm (ε ~ 3.91×10^3 liter $mole^{-1}$ cm^{-1}), and 393 nm (ε ~ 2.71×10^3 liter $mole^{-1}$ cm^{-1}) and for complex **2** significant transition appears at 250 nm (ε ~ 2.37×10^4 liter $mole^{-1}$ cm^{-1}), 312 nm (ε ~ 1.26×10^4 liter $mole^{-1}$ cm^{-1}), and 398 nm (ε ~ 2.40×10^3 liter $mole^{-1}$ cm^{-1}).

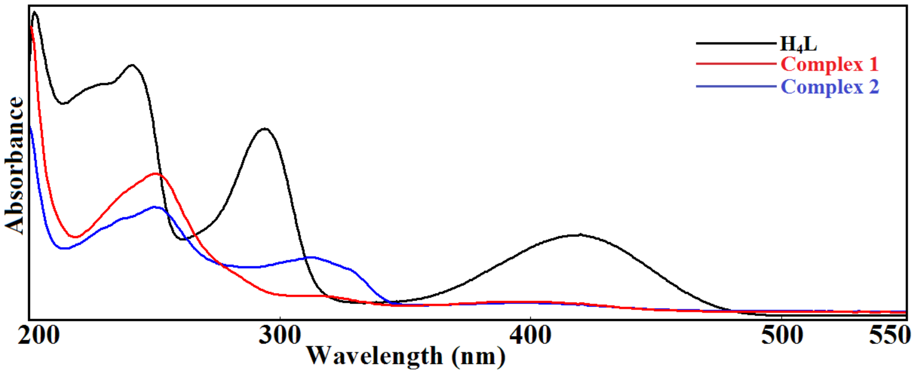

Figure 2.17. UV-Vis absorption spectra of H_4L, 1 and 2.

2.3.5. ESI mass spectrometry

ESI mass spectra of H_4L and complex **1, 2** are recorded in methanol (Figure 2.18). The ESI mass spectrometric data of H_4L shows a peak at m/z = 256.118, which corresponds to $[C_{12}H_{17}NO_5 + H]^+$ mono cation, confirm the chemical composition of ligand. The mass spectra of complex **1** contain a base peak at m/z = 567.142 (calc. 566.704), which can be assigned to $[C_{24}H_{32}CoN_2O_{10} + H]^+$ (calc. 566.704) and is also found in complex **2** at m/z = 567.143. On the other hand the ESI mass spectrometric data of complex **1**, **2** shows two main peaks at m/z = 256.118 and 625.112, these peaks can be assigned to $[C_{12}H_{17}NO_5 + H]^+$ and $[C_{24}H_{30}Co_2N_2O_{10} + H]^+$ mono cations, respectively.

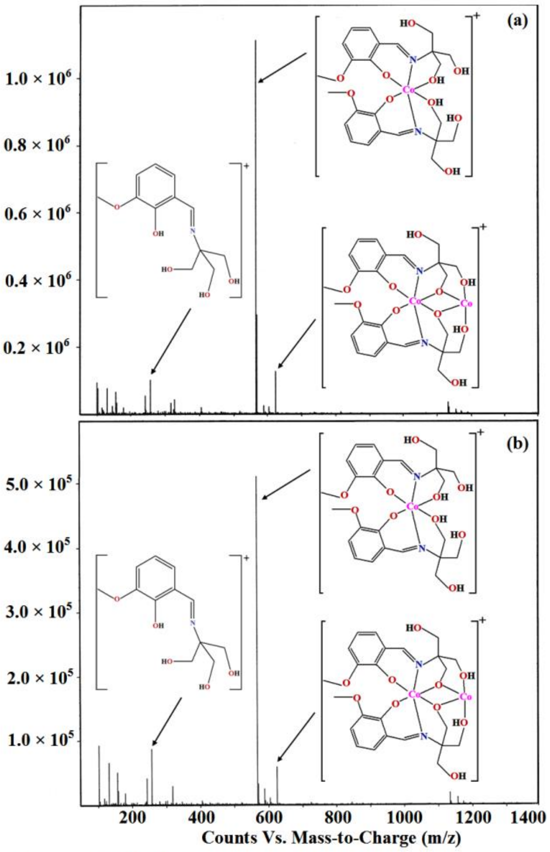

Figure 2.18. ESI-mass spectra of complex 1 (a) and 2 (b) recorded in methanol.

2.3.6. BVS calculation for complexes 1 and 2

In order to confirm these oxidation state of metal centers, bond valence sum (BVS)[2.35a] calculations were performed for each cobalt center; indeed, the BVS calculations for Co2 (2.061) and Co1 (3.48) for compound **1** and for compound **2** these values are Co2 (2.065) and Co1 (3.50), agreed with the +2 and +3 oxidation state (Table 2.6).

$$\mathrm{BVS} = \Sigma s_{ij} = \Sigma exp(r_o - r_{ij})/\mathrm{b}$$

Where s_{ij} is the bond valence between two atoms i and j. r_{ij} is the observed bond length between i and j. r_0 is the bond valence parameter obtained from published tables [2.35b, 2.35c] and b is usually taken as 0.37.

Table 2.6. BVS results for complexes 1 and 2.

	Bond length	1	2
R_0	Co(2)-O(1)	2.05(2)	2.0213(14)
	Co(2)-O(2a)	2.028(3)	2.0379(13)
	Co(2)-O(2b)	2.050(3)	2.0235(12)
1.692	Co(2)-O(3a)	2.192(3)	2.1971(14)
	Co(2)-O(3b)	2.155(3)	2.1895(14)
	Co(2)-O(1w)	2.078(3)	2.0904(15)
	BVS	2.061	2.065
R_0	Bond length	1	2
	Co(1)-N(1a)	1.889(3)	1.8861(15)
1.68	Co(1)-N(1b)	1.887(3)	1.8899(15)
	Co(1)-O(1a)	1.885(3)	1.8749(12)
	Co(1)-O(1b)	1.899(3)	1.9005(13)
1.70	Co(1)-O(2a)	1.915(2)	1.9123(12)
	Co(1)-O(2b)	1.894(3)	1.8870(12)
	BVS	3.48	3.509

2.3.7. PXRD patterns

The powder X-ray diffraction (PXRD) patterns of complexes **1** and **2** are coincident with the diffraction pattern obtained from the single crystal XRD data, suggesting that the bulk sample is same as the single crystal (Figure 2.19 and 2.20).

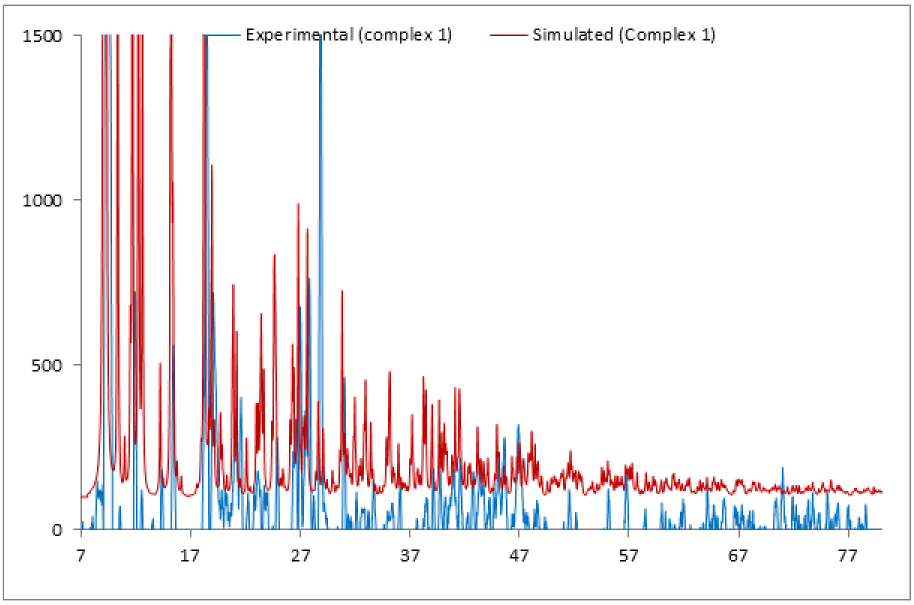

Figure 2.19.Experimental and simulated X-ray powder diffraction pattern of complex **1**.

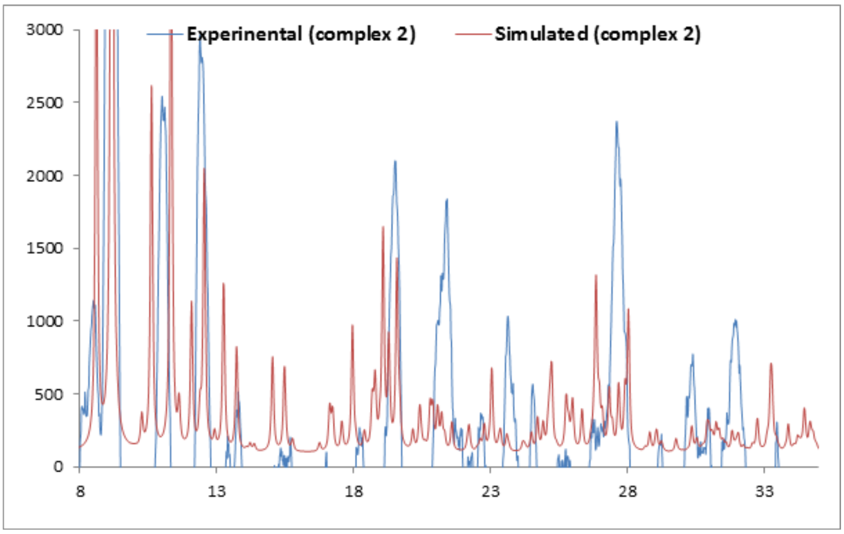

Figure 2.20.Experimental and simulated X-ray powder diffraction pattern of complex **2**.

2.4. Conclusions

In summary, it is presented here the syntheses, crystal structures, and low temperature magnetic behaviors of two new Co^{II}–Co^{III} mixed-valence complexes containing a multidentate Schiff base ligand and dicarboxylate ligands. Magnetic studies demonstrated that the individual Co^{II}–Co^{III} units exhibit field-induced slow magnetic relaxation consistent with SIM behavior. Ab initio NEVPT2 calculations indicate that large axial and rhombic zfs values for the cobalt(II) units are responsible for the particular magnetic behavior of both compounds studied.